Chapter 4

# Micro structural, electrical, magnetic and spectroscopic properties of $PbO\text{-}Sb_2O_3\text{-}As_2O_3$: MnO glass ceramics


## Abstract

*$PbO\text{-}Sb_2O_3\text{-}As_2O_3$ glasses mixed with different concentrations of MnO (ranging from 0 to 5.0 mol %) were crystallized. The samples were characterized by X-ray diffraction, scanning electron microscopy and differential thermal analysis techniques. Dielectric properties over a range of frequency and temperature, optical absorption, fluorescence IR, ESR and magnetic susceptibility at room temperature have been studied. The X-ray diffraction studies have revealed the presence of $Pb_5Sb_2O_8$, $PbSb_2O_6$, $SbAsO_4$, $Mn_2Sb_2O_7$, $Mn_3Sb_2O_6$, $Mn_2O_3$, $MnAsO_4$ and $Pb_5Sb_4O_{11}$ crystalline phases in these samples. The DTA studies have indicated the spreading of the crystallization from inside to the surface of the samples as the concentration of the crystallizing agent is increased. The IR studies have pointed out the existence of conventional $AsO_3$, $SbO_3$, structural units in the glass ceramic samples. These studies have further indicated the decreasing concentration of symmetrical structural vibrational groups with increase in the concentration of MnO. The results of various studies viz., optical absorption, ESR, luminescence and magnetic susceptibility studies have also been reported. The results are analyzed in the light of different oxidation states and environment of manganese ions in the glass ceramic network.*

# Micro structural, electrical, magnetic and spectroscopic properties of $PbO\text{-}Sb_2O_3\text{-}As_2O_3$: MnO glass ceramics

## 4.1 Introduction

Among various transition metal ions, manganese ion is an interesting ion and is extensively investigated in various glasses and glass ceramics. This ion normally exists in $Mn^{2+}$ and $Mn^{3+}$ stable states. $Mn^{2+}$ ion has half filled d orbital with $d^5$ configuration and $^6S$ as its ground state. For these reasons, the total orbital angular momentum for $Mn^{2+}$ ion is zero. Since the total spin is 5/2, this ion exhibits zero field splitting which is sensitive to the local environment. Both $Mn^{3+}$ and $Mn^{2+}$ ions are well known paramagnetic ions. $Mn^{3+}$ ion has a large magnetic anisotropy due to its strong spin-orbit interaction of the 3d orbital where as such anisotropy energy of $Mn^{2+}$ ion is small because its orbital angular momentum is zero.

The influence of manganese ions on optical, magnetic and electrical properties of various inorganic glass systems has been under extensive investigation in recent years [1-3]. Ardelean et. al., have carried out a commendable work on the structural role of manganese ions in a variety of glass systems *viz*., $Bi_2O_3$, phosphate, arsenate etc., [4-6]. A considerable number of studies on the role of manganese ions on physical properties of a diversified glass systems like tellurite, arsenate, phosphate, borate etc., have

also been reported from our laboratory in recent years [7-9]. $Zn_2SiO_4$ crystal is considered as the most suitable host for manganese doping for the luminescence emission [10, 11]. Recently the lasing action of $Mn^{2+}$ ions has also been observed in some of the inorganic glasses [12-15] with large quantum luminescence efficiencies even at room temperature. The studies on up-conversion emission with manganese ion as sensitizer and rare-earth ions as activators in some different glasses have also been reported earlier [16-18]. The manganese ions have larger oscillator strengths than rare-earths and can therefore absorb more of the input energy and fluoresce strongly in the visible region [19-21].

The $Mn^{3+}$ and $Mn^{2+}$ ions exist in different coordinations in glass matrices, for example in borate glasses $Mn^{3+}$ linked in octahedral coordination. In silicate and germinate glasses $Mn^{2+}$ ion reported to be in both tetrahedral and octahedral environment [22]. The tetrahedral and as well as the octahedral $Mn^{2+}$ ions have been found to exhibit luminescence emission in the green and red regions respectively in several glasses [23-25].

The rigorous literature survey on the glass systems containing manganese ions has indicated that in some borate glasses when MnO is present in low concentrations, the manganese ions are reported to be in tetrahedral positions whereas in high concentration range, the ions are

identified to occupy octahedral positions [7]. Similarly, the ESR studies of fluoride glasses containing $Mn^{2+}$ ions have indicated that the local environment of $Mn^{2+}$ ions are very different since $Mn^{2+}$ ions can be incorporated in positions with a broad distribution of Mn-F distance; as a consequence several possible positions were predicted for $Mn^{2+}$ ions in fluoride glasses [9]. Likewise, the structural probing of $Mn^{2+}$ ions in some silicate glasses indicated that, when the concentration of these ions is very low, they take part in well defined tetrahedral sites [26]. The recent studies on the role of $Mn^{2+}$ ions in arsenate glasses indicated that when the manganese oxide is present in the glass matrix at concentrations greater than 0.5 mol %, the manganese ions mostly exist in $Mn^{3+}$ state and take network forming positions [8].

$Mn^{2+}$ has the electronic configuration $3d^5$, which corresponds to a half filled d shell. Most $Mn^{2+}$ complexes are octahedral and have a high spin arrangement with five unpaired electrons. The $d^5$ electronic configuration has a $^6S_{5/2}$ ground state in the free atom and possesses zero orbital angular momentum and hence an ESR signal is expected with ‘g’ value very close to the free electron value 2.0023. $Mn^{2+}$ ions are widely studied as good structural probes in glasses because their ESR spectrum can be easily observed even at room temperature.

Among various conventional crystallizing agents, MnO is expected to be more effective mineralizer especially in the glass systems like antimony-arsenate. Further the inclusion of Mn ions into the antimony glass ceramic network is an added advantage to use these materials for optically operated devices, since unfilled d-shells of these ions contribute more strongly to the non-linear polarizabilities [27]. A considerable number of recent studies on a variety of materials with MnO as nucleating agent are available in the literature [28-31], however such studies on PbO-$Sb_2O_3$-$As_2O_3$: MnO glass ceramics are virtually nil.

This part of the thesis deals with the investigations of (i) bulk crystallization of PbO-$Sb_2O_3$-$As_2O_3$ glasses in the presence of MnO nucleant, (ii) the effect of the concentration of MnO on the crystallization behavior and microstructure of glass ceramic products produced by means of XRD, SEM, DTA and EDS and (iii) the spectroscopic (optical absorption, photoluminescence, ESR and IR), magnetic and dielectric properties.

## 4.2 Brief review of previous work on glasses and glass ceramics containing manganese ions

Krishna et al [32] have studied the structural investigations of $Mn^{2+}$ ions in alkali barium borophosphate glasses by EPR and optical absorption techniques. They have observed $Mn^{2+}$ EPR hyperfine sextet centered at g = 2 and broad absorption bands in the absorption spectra of $Mn^{2+}$ ions; from these results they have concluded that the symmetry around $Mn^{2+}$ ions is octahedral in the glass network and the nature of the bonding character was dominantly ionic. Bogomolova et al [33] have analyzed EPR spectrum of $Mn^{2+}$ ions in fluorogermanate and fluoride glasses using rhombic spin Hamiltonian (and observed an hyperfine sextet centered at g = 2). Van Die et al [34] have also investigated luminescence properties, optical absorption and decay mechanisms of $Mn^{2+}$ ions in germanate glasses; in their studies, the $Mn^{2+}$ emission spectrum was observed to be red shifted to 700 nm. Jean Michael et al [35] have also performed EPR experiments of $Mn^{2+}$ ions in fluoroaluminate glasses and concluded that the divalent manganese ions occupy octahedral distorted sites. Baiocchi et al [36] have reported optical and magnetic properties of manganese ions in lead silicate glasses; using Tanabe Sugano diagrams they have assigned the bands observed in the optical absorption spectrum to the appropriate transitions. Jethwa et al [37]

have studied the possibility of obtaining laser action from $Mn^{2+}$ ions in phosphate glasses. Kashif et al [38] have reported magnetic susceptibility of lithium borosilicate glasses containing manganese ions. Wang et al [39] have studied $Mn^{2+}$ luminescence in phosphate glasses. Lakshmana Rao et al [40] have reported the changes in the ESR and optical absorption spectra of $Mn^{2+}$ ions in $Na_2SO_4$-$ZnSO_4$ glasses with the change in concentration. They have calculated crystal field and Racah parameters and from these studies they concluded that $Mn^{2+}$ ions occupy octahedral sites in these glasses. Qiang Su et al [41] have also investigated the Photo-stimulated long lasting phosphorescence in Mn2+ doped zinc borosilicate glasses. Stefan and Simon [42] investigated EPR of $Mn^{2+}$ ions doped bismuth borate glasses and structural data obtained from these measurements indicate various sites for $Mn^{2+}$ ions in environments characterized by different crystalline field intensities. Ardelean et al [43] have studied the valence states of manganese ions and the interactions involving them for MnO containing $Bi_2O_3$-PbO-$As_2O_3$ glasses by means of the temperature dependence of the magnetic susceptibility and concluded that at lower concentrations manganese exists in both $Mn^{2+}$ and $Mn^{3+}$ states while at higher concentrations divalent valence state dominates.

Though, a considerable number of studies on some MnO glasses and glass ceramics are available, still there is a lot of scope to investigate the role of manganese ions on the structural aspects of especially in PbO-$Sb_2O_3$-$As_2O_3$ glass ceramics on dielectric and other physical properties.

Within the possible glass forming region of PbO-$Sb_2O_3$-$As_2O_3$ system, a particular compositions 40PbO–20$Sb_2O_3$–40$As_2O_3$ is chosen for the present study. The crystallizing agent MnO is varied from 0 to 5.0 mol% in this glass matrix. The detailed compositions are as follows:

$Mn_0$: 40PbO–20$Sb_2O_3$–40$As_2O_3$

$Mn_1$: 40PbO–19$Sb_2O_3$–40$As_2O_3$: 1.0 MnO

$Mn_2$: 40PbO–18$Sb_2O_3$–40$As_2O_3$: 2.0 MnO

$Mn_3$: 40PbO–17$Sb_2O_3$–40$As_2O_3$: 3.0 MnO

$Mn_4$: 40PbO–16$Sb_2O_3$–40$As_2O_3$: 4.0 MnO

$Mn_5$: 40PbO–15$Sb_2O_3$–40$As_2O_3$: 5.0 MnO

The glass specimens prepared (with the procedure described in Chapter 2 ) with various concentrations of MnO were heat treated in a furnace at 300 $^oC$ for 6 h and chilled to room temperature for the crystallization.

## 4. 3 Characterization

### *4.3.1 Scanning electron microscopy*

Fig. 4.1 shows SEM pictures of the some of the $PbO–Sb_2O_3–As_2O_3$: MnO glass ceramic samples; the pictures clearly indicate that the samples contain well defined and randomly distributed crystal grains. The residual glass phase may be acting as interconnecting zones among the crystallized areas making the samples free of voids and cracks.

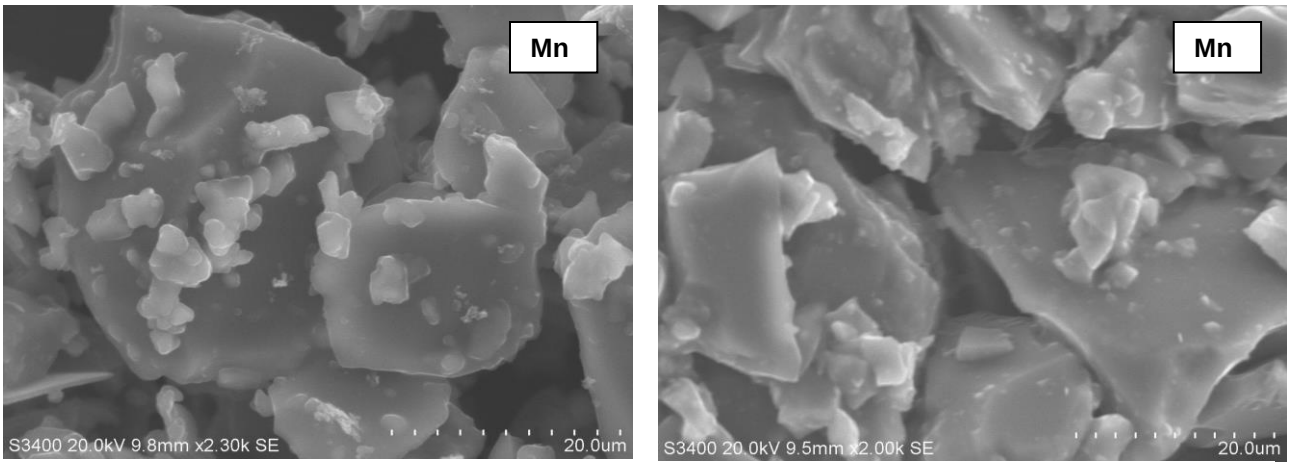


Fig 4.1 SEM images for some of the crystallized $PbO\text{-}Sb_2O_3\text{-}As_2O_3$: MnO glasses

### *4.3.2 Energy dispersive spectroscopy*

The chemical makeup of the glass ceramics is characterized by electron dispersive spectroscopy (EDS); the energy analysis of the glass ceramic materials indicates lead, arsenic, antimony and manganese elements in various crystalline phases (Fig. 4.2).

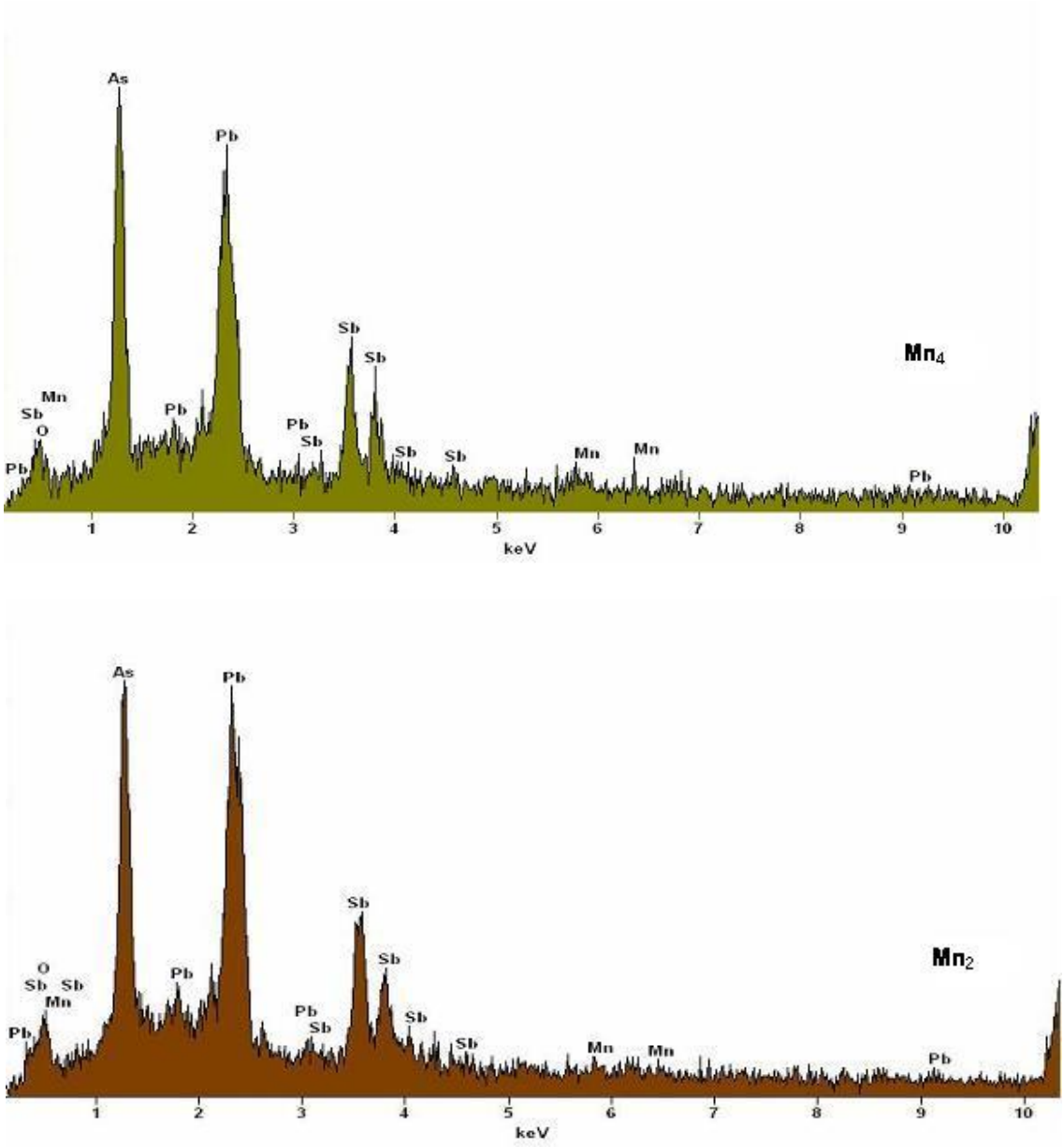


Fig 4.2 EDS spectra of some of the $PbO\text{-}Sb_2O_3\text{-}As_2O_3$: MnO glass ceramics.

### *4.3.3 X-ray diffraction*

The X-ray diffraction analysis of the pre-heated PbO-$Sb_2O_3$-$As_2O_3$: MnO glass samples shows that the samples prepared are of amorphous in nature. XRD patterns of glass ceramic samples (Fig. 4.3) exhibit micro-structural changes.

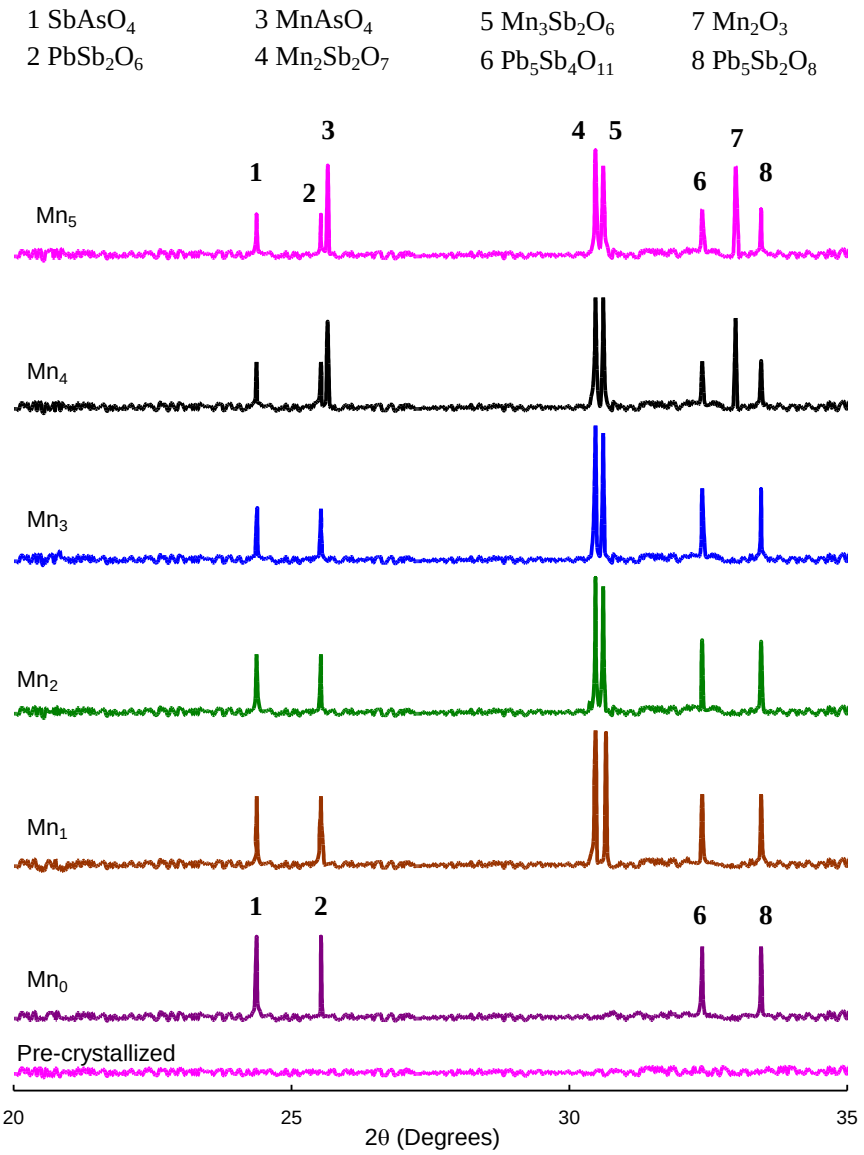


Fig. 4.3 XRD patterns of PbO-$Sb_2O_3$-$As_2O_3$: MnO glass ceramics.

$Pb_5Sb_2O_8$, $PbSb_2O_6$, $SbAsO_4$, $Mn_2Sb_2O_7$, $Mn_3Sb_2O_6$, $Mn_2O_3$, $MnAsO_4$ and $Pb_5Sb_4O_{11}$ that are kinetically and thermodynamically feasible seemed to be the main crystalline products in these samples. The patterns indicate that antimony ions exist in $Sb^{5+}$ oxidation state in addition to $Sb^{3+}$ state. Similarly the crystalline phases of $Mn^{3+}$ ions also detected in addition to $Mn^{2+}$ phases.

### *4.3.4 Differential thermal analysis*

Fig. 4.4 shows the differential thermal analysis traces for some of the PbO–$Sb_2O_3$–$As_2O_3$: MnO glass ceramic samples. All the traces indicate typical glass transition with the inflection point between 255-290 $^oC$. It is observed that glass transition temperature is slightly decreasing for these samples with the increasing content of MnO. At nearly 380 $^oC$, process of crystallizations begins; the thermograms of various glass ceramic samples crystallized with higher quantities of MnO (beyond 2 mol%) exhibited two well-defined exothermic peaks at the two steps of crystallization temperatures (peaks) followed by an endothermic peak – due to re-melting of the samples. Similar to glass-transition temperature (Tg), the crystallization temperatures and melting points of all samples varied with change of MnO content. From the pattern of the crystallization peaks, it appears that the enthalpy associated with the crystallization increases with the concentration of crystallizing agent. The inset of Fig. 4.4 represents typical DTA/TG trace for one of

the sam ould clearly be seen during heating

process ccessive steps. First,

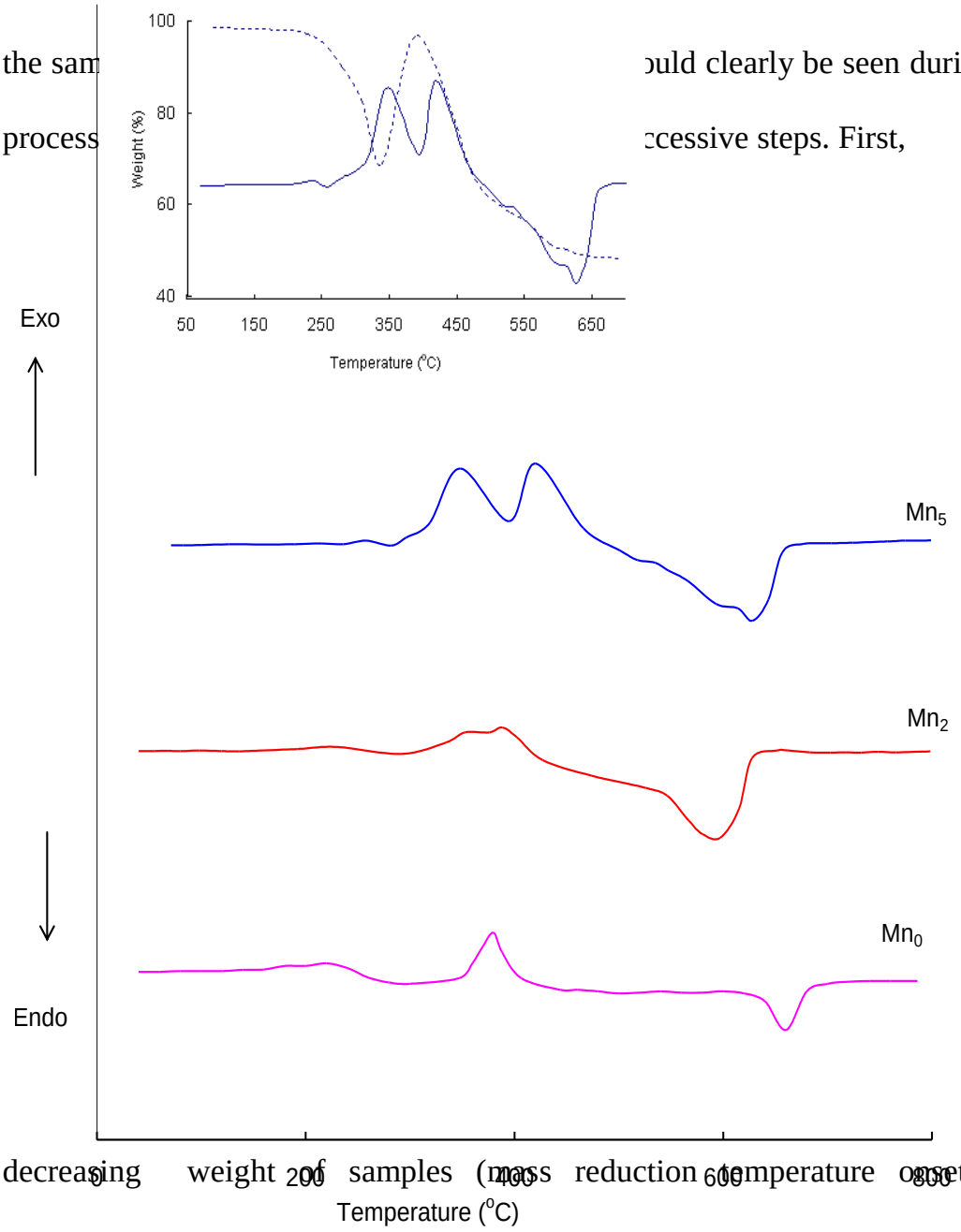


decreasing weight of samples (mass reduction temperature onset), second increasing of weight up to mass increase temperature peak and rapid mass lowering to residual mass.

Fig. 4.4 DTA traces for some of the $PbO$-$Sb_2O_3$-$As_2O_3$: $MnO$ glass ceramics. Inset represents typical DTA/TG trace for glass ceramic $Mn_5$.

The mass increasing peak is well corresponding to the crystallization peak. The thermograms of all other samples have also exhibited similar behavior. The TG

measurements further indicated shifting of the maximum mass reduction temperature towards lower side with increase in the MnO content. The pertinent data related to differential thermal analysis of the samples is presented in Table 4.1.

**Table 4.1**

Summary of the data on differential thermal analysis studies of $PbO$-$Sb_2O_3$-$As_2O_3$: MnO glass ceramics

| Glass ceramic | MnO conc. (mol%) | Glass transition temp. ($^oC$) (Inflection) | Cryst. temp. (peak) ($^oC$) First step | Melting temp. ($^oC$) |
|---|---|---|---|---|
| $Mn_1$ | 1.0 | 254 | 354 | 590 |
| $Mn_2$ | 2.0 | 252 | 352 | 598 |
| $Mn_3$ | 3.0 | 251 | 350 | 605 |
| $Mn_4$ | 4.0 | 249 | 349 | 615 |
| $Mn_5$ | 5.0 | 247 | 348 | 628 |

### 4.3.5 *Physical parameters*

The density of the MnO free glass ceramic material is measured to be 5.790 $g/cm^3$. The gradual increase of crystallizing agent MnO in the glass matrix caused a slight decrease in the density (Table 4.2). From the measured values of the density

and average molecular weight $\overline{M}$ of the samples, various other physical parameters such as manganese ion concentration $N_i$, mean manganese ion separation $r_i$, polaron radius $r_p$ in $PbO\text{-}Sb_2O_3\text{-}As_2O_3$: MnO glass ceramics are computed and presented in Table 4.2.

**Table 4.2**

The physical properties of $PbO\text{-}Sb_2O_3\text{-}As_2O_3$: MnO glass ceramics.

| Property ↓ /Sample → | $Mn_0$ | $Mn_1$ | $Mn_2$ | $Mn_3$ | $Mn_4$ | $Mn_5$ |
|---|---|---|---|---|---|---|
| Density d ($g/cm^3$) | 5.790 | 5.855 | 5.847 | 5.835 | 5.822 | 5.809 |
| Average molecular weight $\overline{M}$ | 226.72 | 224.51 | 222.30 | 220.10 | 217.89 | 215.69 |
| $Mn^{2+}$ ion conc. $N_i$ ($10^{22}$ ions/$cm^3$) | - | 1.56 | 3.15 | 4.79 | 6.47 | 8.17 |
| Inter ionic distance of Mn ions $r_i$ ($A^o$) | - | 4.00 | 3.16 | 2.75 | 2.49 | 2.30 |
| Polaron radius $r_p$ ($A^o$) | - | 1.61 | 1.27 | 1.11 | 1.00 | 0.93 |

## 4.4 Results

### *4.4.1 Optical absorption spectra*

Fig. 4.5 shows the optical absorption spectra of $PbO–Sb_2O_3–As_2O_3$: MnO glass ceramics in the wavelength region of 380-600 nm. The absorption edge observed at 382.5 nm for the MnO free sample is found to be shifted gradually towards higher wavelength with increase in the concentration of nucleating agent. In addition, the spectrum of the sample $Mn_1$ exhibited two absorption bands at 520 nm and 422 nm respectively corresponding to the transitions $^6A_{1g}(S) \rightarrow {}^4T_{1g}(G)$ and $^6A_1\ (S) \rightarrow {}^4T_2\ (G)$ of $Mn^{2+}$ ions. To be more precise, the first band is identified due to the octahedral transition where as the second one is due to the tetrahedral transition of $Mn^{2+}$ ions [43-45]. With increase in the concentration of crystallizing agent MnO up to 5.0 mol %, the octahedral band is observed to grow at the expense of the tetrahedral band and a new absorption band with peak at about 490 nm is appeared. This new band is identified due to $^5E_g \rightarrow {}^5T_{2g}$ transition of $Mn^{3+}$ ions [46]. The summary of data on the positions of various bands in the optical absorption spectra of $PbO–Sb_2O_3–As_2O_3$: MnO glass ceramics are presented in Table 4.3

From the observed absorption edges, we have evaluated the optical band gaps ($E_o$) of these glasses by drawing Urbach plot (Fig. 4.6) between ($\alpha$

$\hbar\omega)^{1/2}$ and $\hbar\omega$. The values of optical band gap ($E_o$) obtained are presented in Table 3. The lowest optical band gap is observed for the sample $Mn_5$.

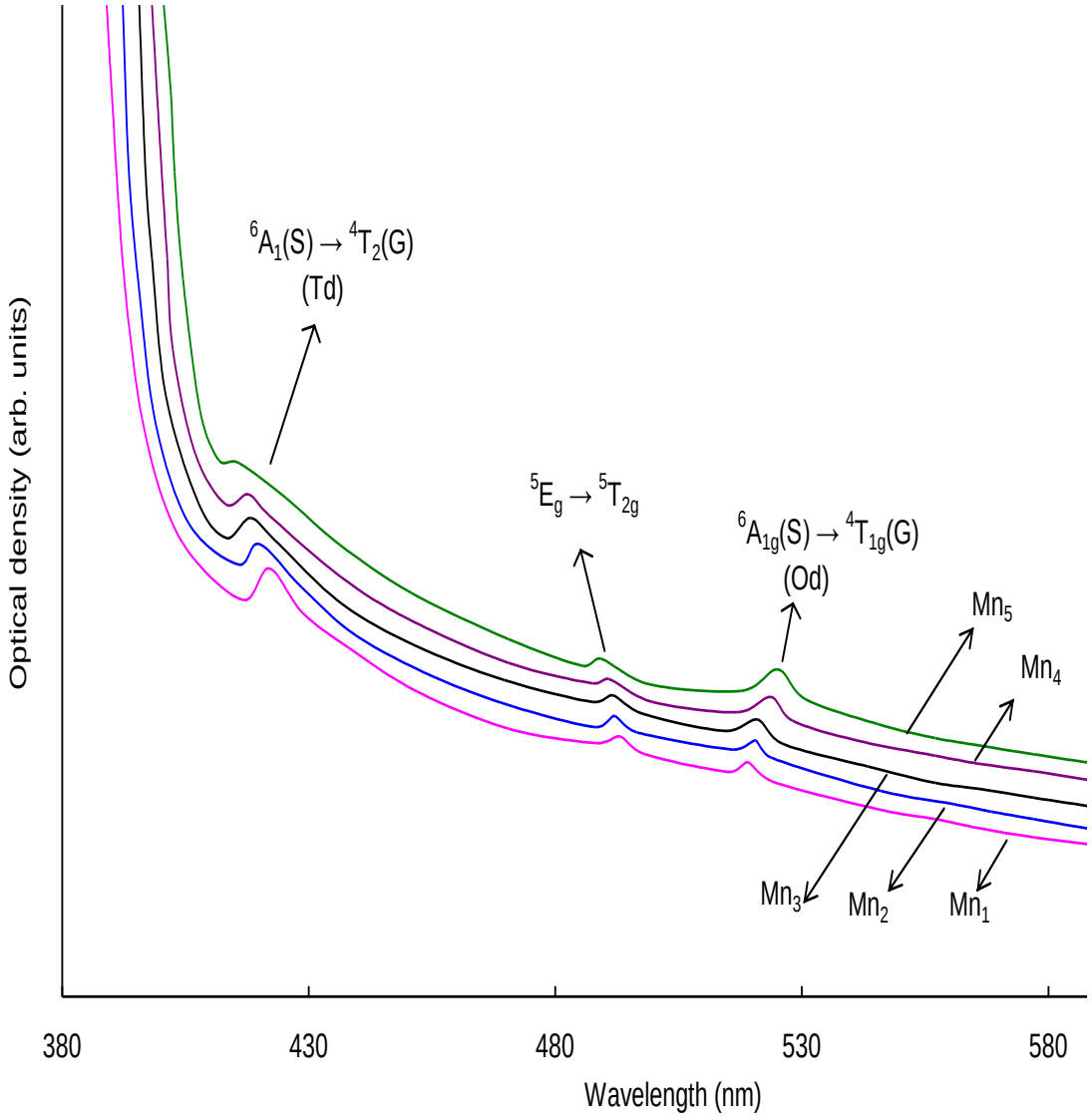


Fig. 4.5 Optical absorption spectra of $PbO\text{-}Sb_2O_3\text{-}As_2O_3$: MnO glass ceramics.

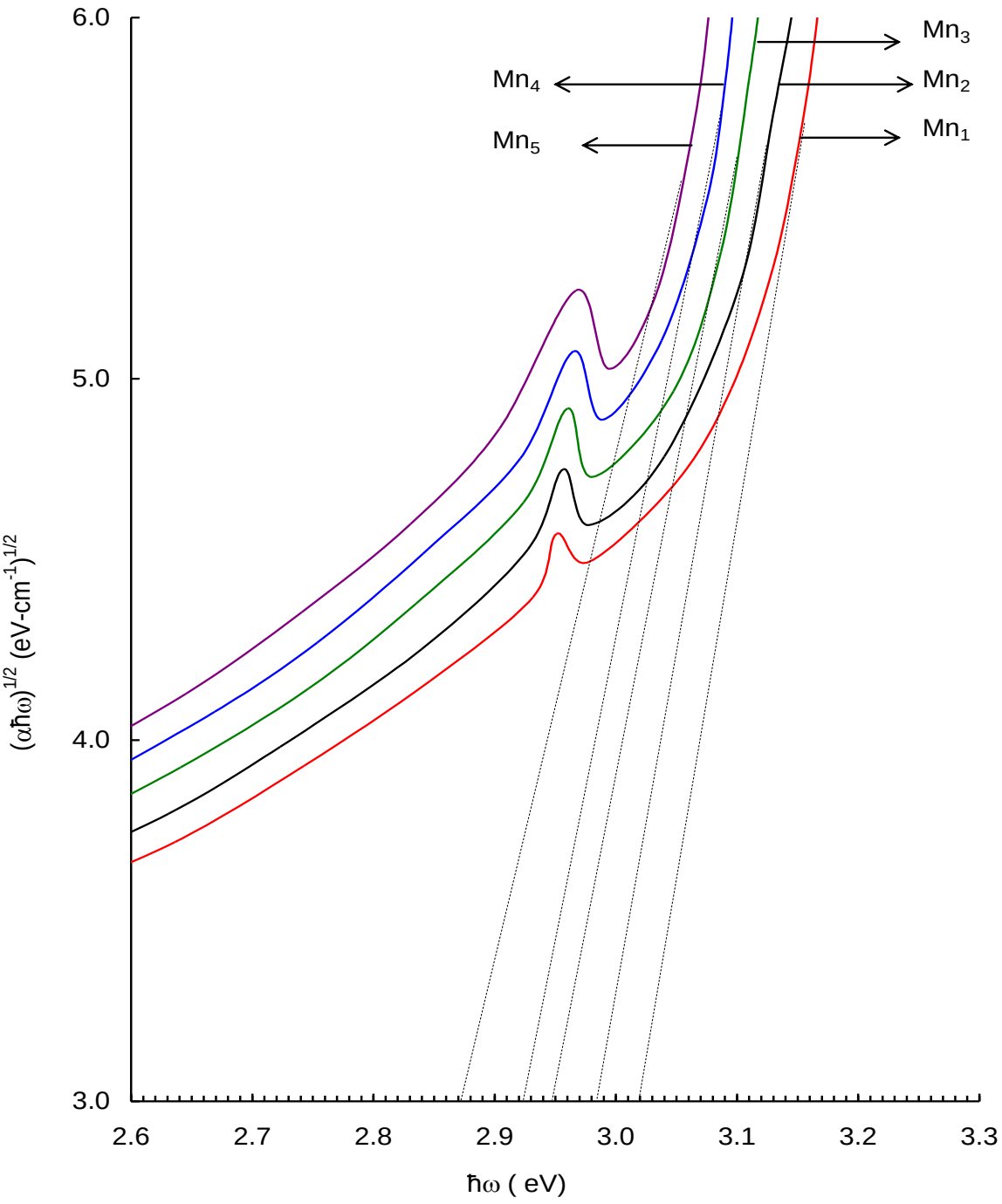


Fig. 4.6 Plots to evaluate optical band gaps for $PbO\text{-}Sb_2O_3\text{-}As_2O_3$: MnO glass ceramics.

**Table 4.3**

Summary of data on optical absorption spectral data of $PbO\text{-}Sb_2O_3\text{-}As_2O_3$: MnO glass ceramics.

| Glass ceramic | $Mn_1$ | $Mn_2$ | $Mn_3$ | $Mn_4$ | $Mn_5$ |
|---|---|---|---|---|---|
| $Mn^{2+}$ transitions(nm) | | | | | |
| $^6A_{1g}(S) \rightarrow {}^4T_{1g}(G)$ | 422 | 420 | 418.2 | 417.8 | 416 |
| $^6A_1(S) \rightarrow {}^4T_2(G)$ | 519 | 520.6 | 521 | 523.7 | 525 |
| $Mn^{3+}$ transition (nm) | | | | | |
| $^5E_g \rightarrow {}^5T_{2g}$ | 493 | 492 | 491.6 | 490.5 | 489.2 |
| Cut-off wavelength (nm) | 389 | 392 | 395.6 | 398.2 | 400.6 |
| Optical band gap $E_o$ (eV) | 3.02 | 2.99 | 2.95 | 2.93 | 2.88 |

### 4.4.2 *Excitation and Emission spectra*

The optical excitation spectrum, for one of the samples viz., $Mn_2$, is shown in Fig. 4.7; the excitation spectrum exhibited two distinct bands in the visible region due to d-d transitions of $Mn^{2+}$ ions; from these spectra, $\lambda_{exc}$ is determined as 449 nm and the same was used for recording emission spectra of these glass ceramics. The excitation spectra are observed to similar for the remaining glass ceramics. The emission spectra of all the glass ceramic samples recorded at room temperature are shown in Fig. 4.8. The spectra

exhibited two prominent emission bands at about 550 nm (green emission) and 650 nm (orange emission).

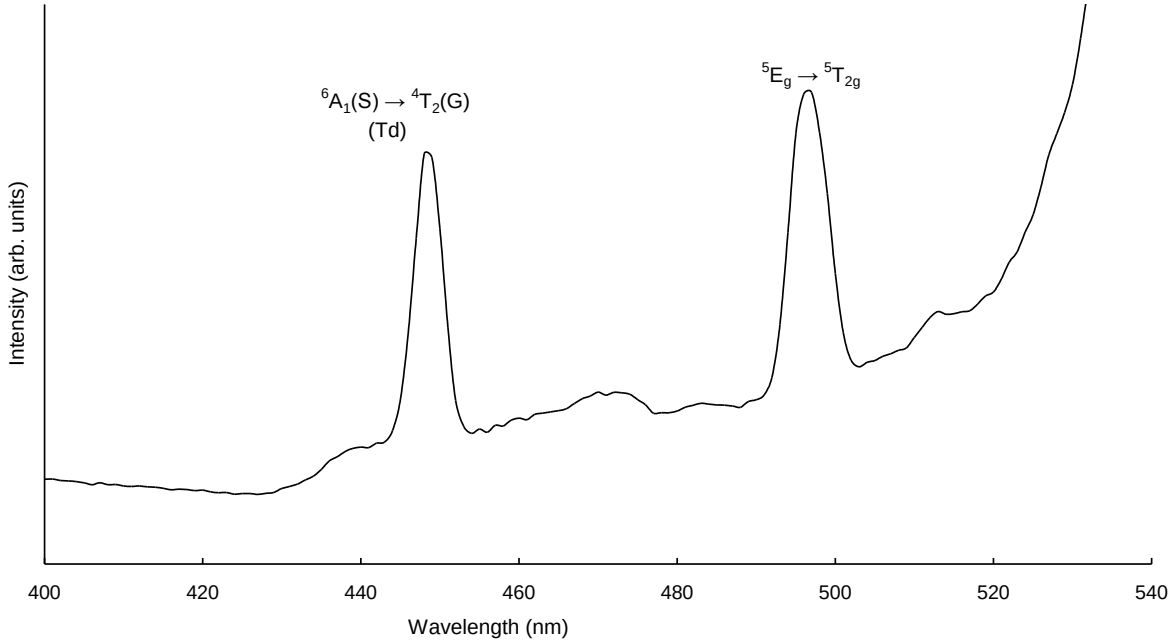


Fig. 4.7 Excitation spectrum of glass ceramic $Mn_2$ recorded at room temperature ($\lambda_{emission}$ = 550 nm).

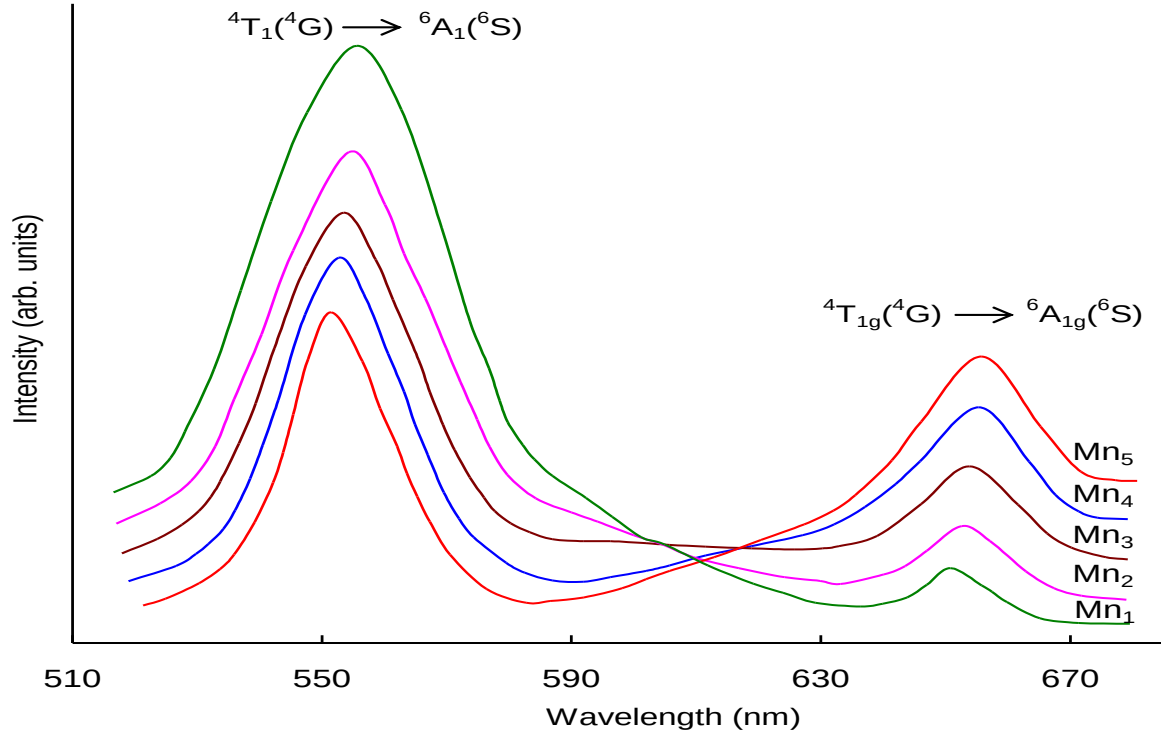


Fig. 4.8 Emission spectra of PbO-$Sb_2O_3$-$As_2O_3$: MnO glass ceramics recorded at room temperature ($\lambda_{exc}$ = 449 nm).

As the concentration of crystallizing agent is increased, the orange emission band is observed to grow at the expense of green emission band.

### *4.4.3 ESR spectra*

No ESR spectral signatures are detected in the MnO free samples. Fig. 4.9 represents the typical ESR spectra of PbO-$Sb_2O_3$-$As_2O_3$ glass crystallized with different concentrations of MnO. The spectra are characterized by six-line hyperfine structure centered at g ~ 2.001 and another signal at g ~ 4.3; the relative intensity of these two signals is observed to increase with increase in the concentration of manganese ions in the samples. However, the spectra of the samples $Mn_1$ and $Mn_2$ do not exhibit any resolution. The values of g obtained for $Mn^{2+}$ ions for the present samples is comparable with that of other systems; for example, $Bi_2O_3$ – $GeO_2$ [6, 47], lead arsenate [8], alkali sulphate glasses [44].

### *4.4.4 Magnetic susceptibility*

Magnetic susceptibility of PbO-$Sb_2O_3$-$As_2O_3$: MnO glass ceramics measured at room temperature is observed to increase with MnO content in the glass composition (Table 4.4). From the values of magnetic susceptibilities, effective magnetic moments of manganese ions in the glasses are evaluated and presented in Table 4.4. The value of $\mu_{eff}$ is found to be the

highest (5.90 $\mu_B$) for glass $Mn_1$ and decreases to a value of 5.60 $\mu_B$ for the glass containing 5.0 mol% of MnO.

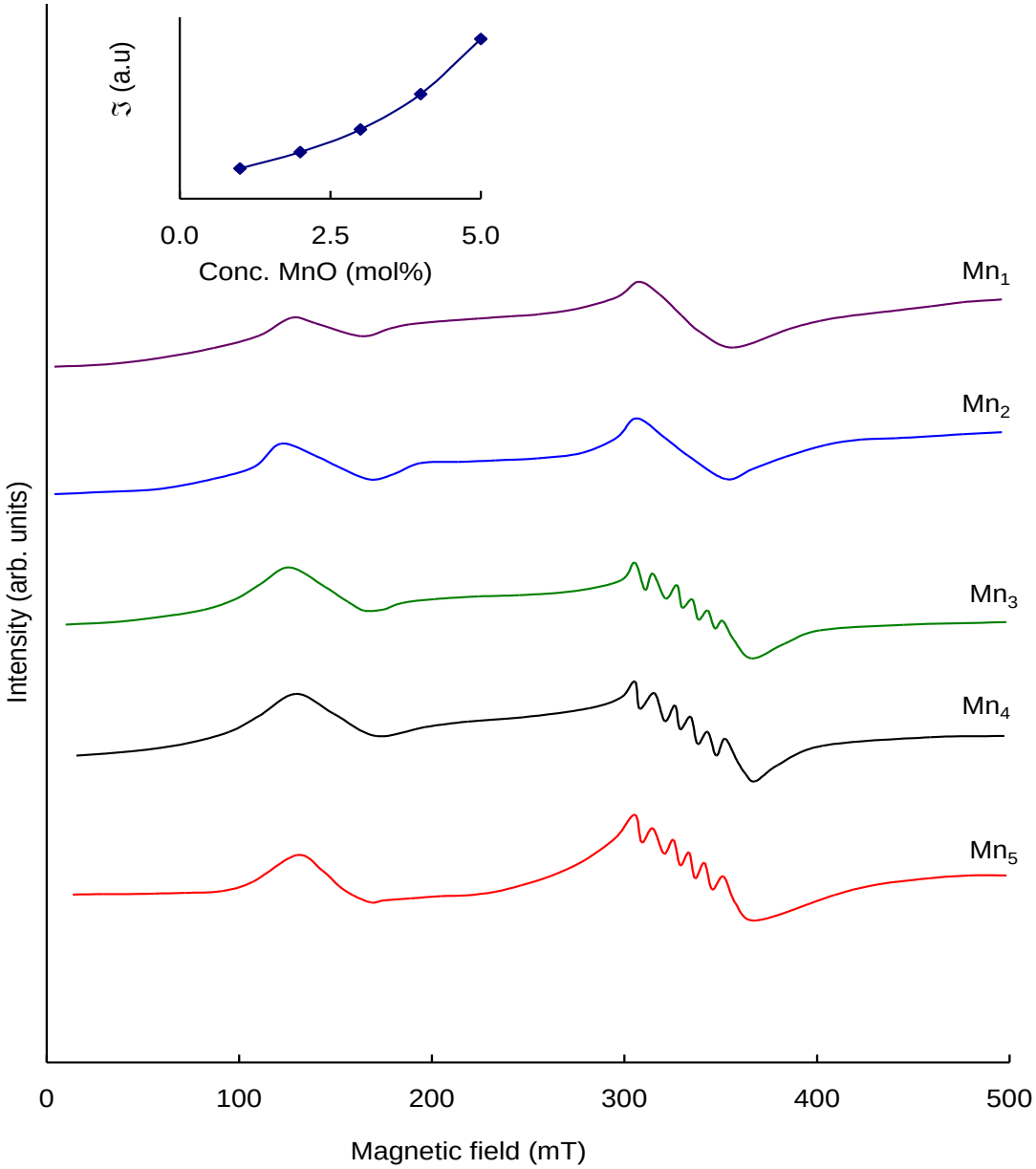


Fig. 4.9 ESR spectra of $PbO\text{-}Sb_2O_3\text{-}As_2O_3$: MnO glass ceramics recorded at room temperature. Inset gives the dependence of intensity factor for g = 2.0 signal with conc. of MnO.

**Table 4.4**

Summary of data on magnetic properties of $PbO\text{-}Sb_2O_3\text{-}As_2O_3$: MnO glass ceramics.

| Glass ceramic | Conc. MnO (mol %) | $\chi$ ($10^{-6}$ emu) | $\mu_{eff}$ ($\mu_B$) | 'g' value of sextet | $x_1$ (approx. % of $Mn^{2+}$ ions) | $x_2$ (approx. % of $Mn^{3+}$ ions) | hfs parameter A (mT) |
|---|---|---|---|---|---|---|---|
| $Mn_1$ | 1.0 | 13.31 | 5.90 | 2.005 | 97.86 | 2.14 | 9.02 |
| $Mn_2$ | 2.0 | 30.20 | 5.89 | 2.003 | 96.79 | 3.21 | 9.20 |
| $Mn_3$ | 3.0 | 49.92 | 5.87 | 1.996 | 94.66 | 5.34 | 9.28 |
| $Mn_4$ | 4.0 | 72.94 | 5.85 | 1.995 | 92.53 | 7.47 | 9.46 |
| $Mn_5$ | 5.0 | 97.10 | 5.60 | 1.981 | 66.60 | 33.40 | 9.88 |

### *4.4.5 IR spectra*

IR spectrum of crystalline $Sb_2O_3$ is expected to exhibit four fundamental absorption bands designated by $\nu_1$ (925 $cm^{-1}$)—due to symmetric stretching vibrations, $\nu_2$ (600 $cm^{-1}$)—due to symmetric bending vibrations, $\nu_3$ (710 $cm^{-1}$)—due to doubly degenerate stretching vibrations and $\nu_4$ (485 $cm^{-1}$)—due to doubly degenerate bending vibrations ($\nu_4$) of $SbO_3$ structural units [48, 49]. In the infrared spectrum of glass ceramic sample $Mn_1$, the band due to $\nu_1$ vibrations of $SbO_3$ structural groups is observed at about 939 $cm^{-1}$ and the band related to $\nu_2$ vibrations of these units is observed at 617 $cm^{-1}$. The IR spectrum of crystalline $As_2O_3$ is also expected to exhibit

four fundamental absorption bands at $\nu_1$ (1050 $cm^{-1}$), $\nu_2$ (618 $cm^{-1}$), $\nu_3$ (795 $cm^{-1}$) and $\nu_4$ (505 $cm^{-1}$) [48]. In the spectrum of glass ceramic $Mn_1$ (Fig. 4.10) , the $\nu_1$ band is appeared at 1025 $cm^{-1}$, where as, the $\nu_2$ bands and the $\nu_3$ bands of $SbO_3$ and $AsO_3$ structural groups are merged and exhibited common meta-centers at 619 and 769 $cm^{-1}$, respectively. In the region of $\nu_4$ vibrations, it is believed that the vibrations due to $PbO_4$ structural groups could also be present; in fact the vibrational band due to $PbO_4$ units was reported at 470 $cm^{-1}$ in a number of other glass systems [50].

As the concentration of the crystallizing agent MnO is increased, the intensity of bands due to symmetric stretching and symmetric bending vibrations of $SbO_3$ and $AsO_3$ structural groups is observed to decrease gradually. Further, the common vibrational band due to $\nu_2$ vibrations of $SbO_3$ and $AsO_3$ structural groups is observed to split in to two separate bands at higher concentrations of the nucleating agent.

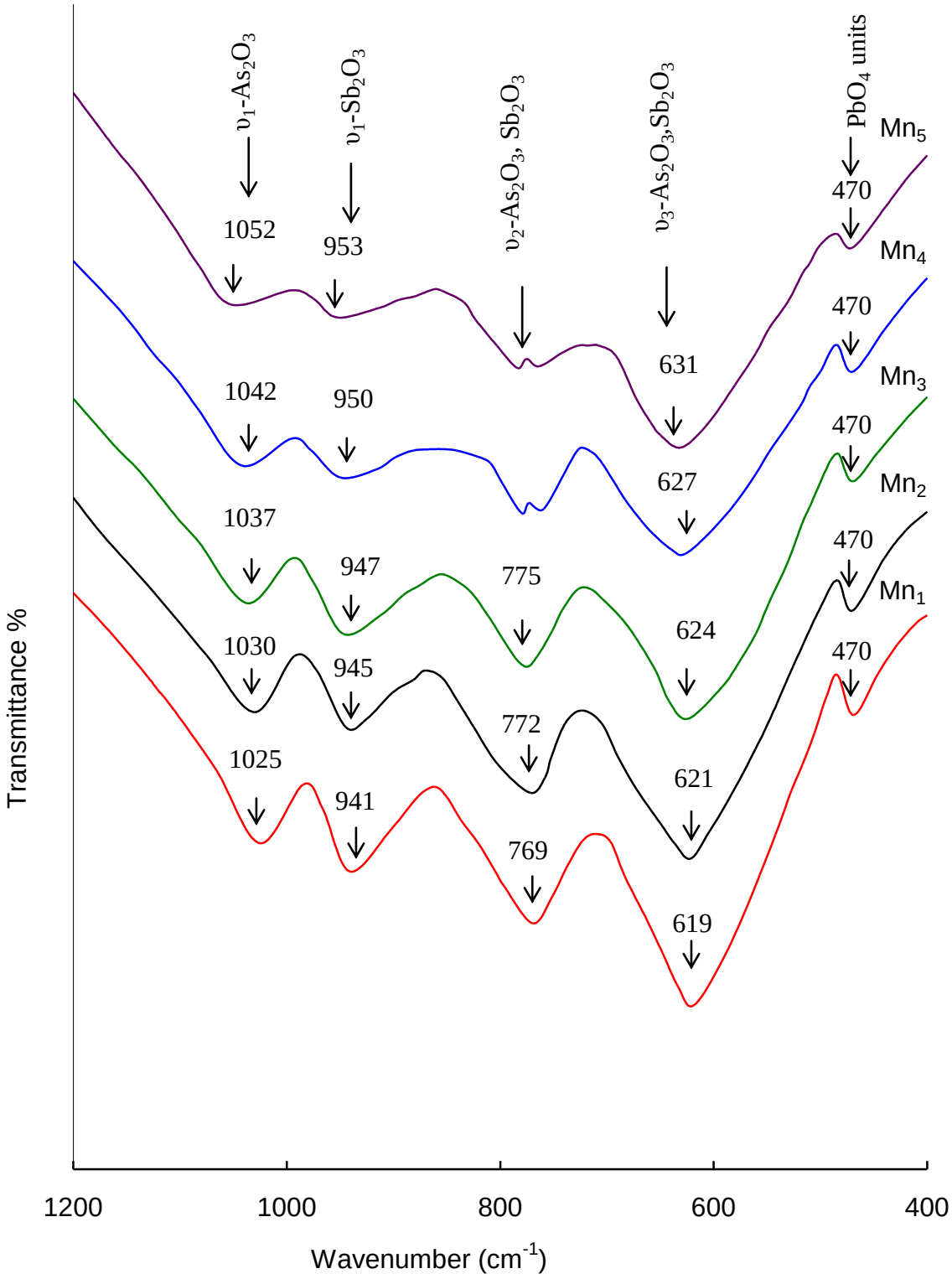


Fig. 4.10 IR spectra of $PbO\text{-}Sb_2O_3\text{-}As_2O_3$: MnO glass ceramics.

### *4.4.6 Dielectric properties*

The dielectric constant ε' and loss tan δ at room temperature ( ≈ 30 $^{o}$C) of PbO- $Sb_2O_3$-$As_2O_3$ glass ceramic at 100 kHz are measured to be 14.7 and 0.005 respectively; these values are found to increase considerably with decrease in frequency. Fig. 4.11 represents the variation of dielectric constant and loss with frequency at room temperature of PbO-$Sb_2O_3$-$As_2O_3$ glasses crystallized with different concentrations of MnO; inset of the same figure shows the variation of these parameters with the concentration of crystallizing agent MnO measured at 1 kHz. The parameters, ε' and tanδ are observed to increase with the concentration of MnO.

The temperature dependence of ε' at 1 kHz of PbO- $Sb_2O_3$-$As_2O_3$ glasses crystallized with different concentrations of MnO is shown in Fig. 4.12 and at different frequencies for one of glass ceramic sample $Mn_4$ is shown as the inset. The value of $\varepsilon^{'}$ is found to exhibit a considerable increase at higher temperatures especially at lower frequencies; however the rate of increase of $\varepsilon^{'}$ with temperature is found to increase with increase in the concentration of crystallizing agent.

A comparison plot of variation of tan δ with temperature, measured at a frequency of 10 kHz for all the glass ceramic samples is presented in Fig. 4.13.

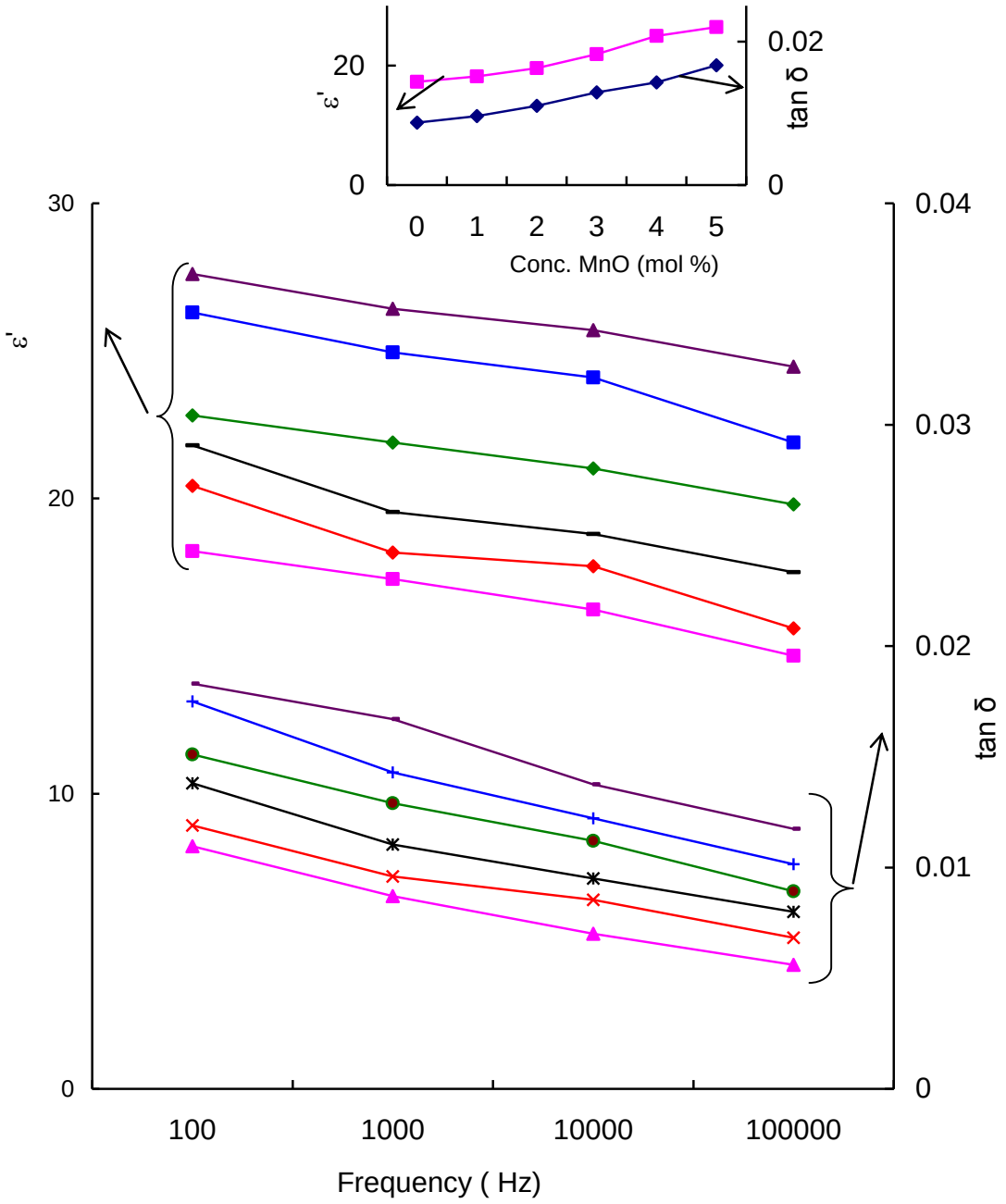


Fig. 4.11 Variation of dielectric constant and loss with frequency of PbO-$Sb_2O_3$-$As_2O_3$: MnO glass ceramics measured at room temperature. Inset represents the variation of dielectric constant and loss at room temperature with the concentration of the crystallizing agent.

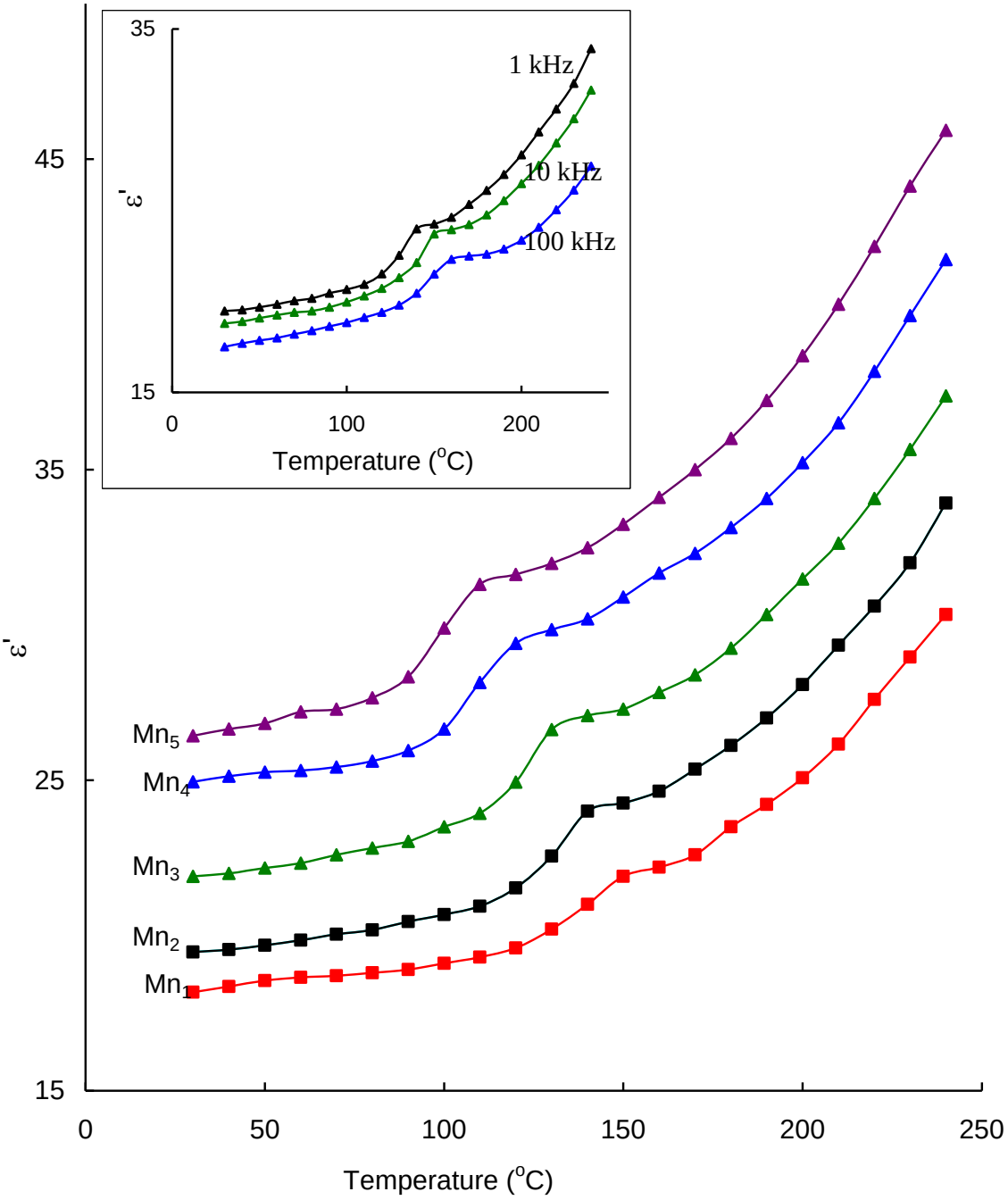


Fig. 4.12 A comparison plot of variation of dielectric constant with temperature at 1 kHz for $PbO\text{-}Sb_2O_3\text{-}As_2O_3$: MnO glass ceramics. Inset gives the variation of dielectric constant with temperature at different frequencies of glass ceramic $Mn_4$.

**The inset of this figure represents the temperature dependence of tan δ of sample $Mn_3$ at different frequencies. The dependence of dielectric loss with temperature at different frequencies exhibits distinct maxima indicating dipolar relaxation character of dielectric loss in these glass ceramic samples. From these curves, it is also observed that the region of relaxation shifts towards lower temperatures with broadening of relaxation peaks and increasing value of $(\tan \delta)_{max}$ with increase in the concentration of the nucleating agent. The effective activation energy $W_d$ for the dipoles is evaluated for all the glass ceramic and presented in Table 4.5; the activation energy is found to decrease gradually with increase in the concentration of the crystallizing agent.**

**Table 4.5**

Data on dielectric loss of PbO- $Sb_2O_3$- $As_2O_3$: MnO glass ceramics.

| Glass ceramic | $(\text{Tan } \delta)_{\text{Max.Avg}}$ | Temp. region of relaxation ($^oC$) | A.E. for dipoles (eV) |
|---|---|---|---|
| $Mn_1$ | 0.0211 | 140-178 | 3.58 |
| $Mn_2$ | 0.0232 | 130-170 | 3.42 |
| $Mn_3$ | 0.0256 | 115-160 | 3.26 |
| $Mn_4$ | 0.0268 | 110-149 | 3.10 |
| $Mn_5$ | 0.0279 | 98-140 | 2.95 |

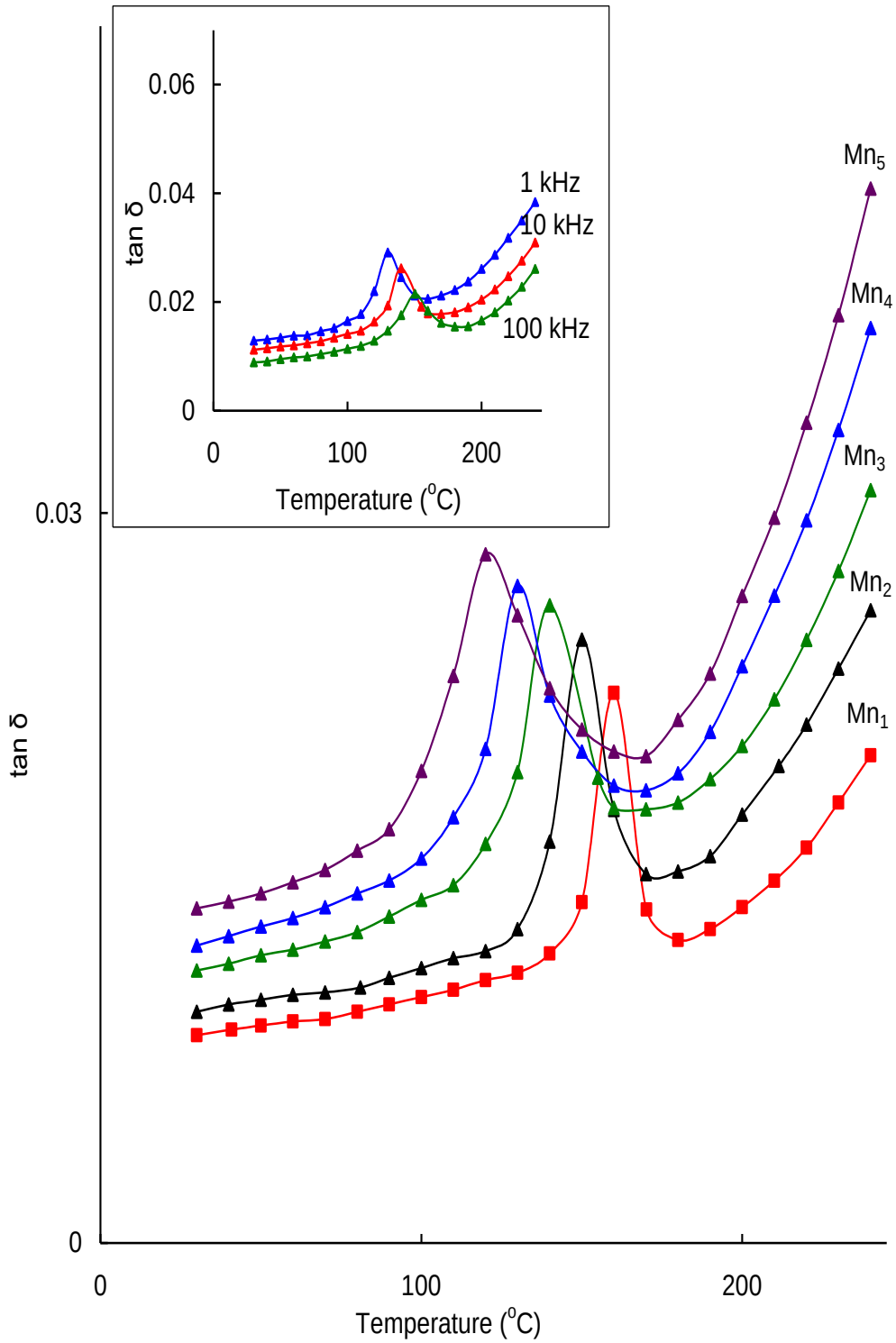


Fig.4.13 A comparison plot of variation of dielectric loss with temperature at 10 kHz for $PbO\text{-}Sb_2O_3\text{-}As_2O_3$: MnO glass ceramics. Inset gives the variation of dielectric loss with temperature at different frequencies of glass ceramic $Mn_3$.

**The a.c. conductivity $\sigma_{ac}$ is calculated at different temperatures, using the relation as given in Chapter 3, for different frequencies and the plots of log $\sigma_{ac}$ against 1/T are shown in Fig. 4.14 for all the glass ceramics at 100 kHz. From these plots, the activation energy for conduction in the high temperature region over which a near linear dependence of log $\sigma_{ac}$ with 1/T could be observed is evaluated and presented in Table 4.6; this activation energy is also found to decrease gradually with increase in the concentration of the crystallizing agent.**

**Table 4.6**

Summary of data on a.c. conductivity of PbO- $Sb_2O_3$-$As_2O_3$: MnO glass ceramics.

| Glass ceramic | $N(E_F)$ ($10^{20}$, $eV^{-}/cm^3$) | A.E. for conduction (eV) |
|---|---|---|
| $Mn_1$ | 1.95 | 0.67 |
| $Mn_2$ | 2.14 | 0.57 |
| $Mn_3$ | 2.48 | 0.50 |
| $Mn_4$ | 2.77 | 0.45 |
| $Mn_5$ | 3.02 | 0.41 |

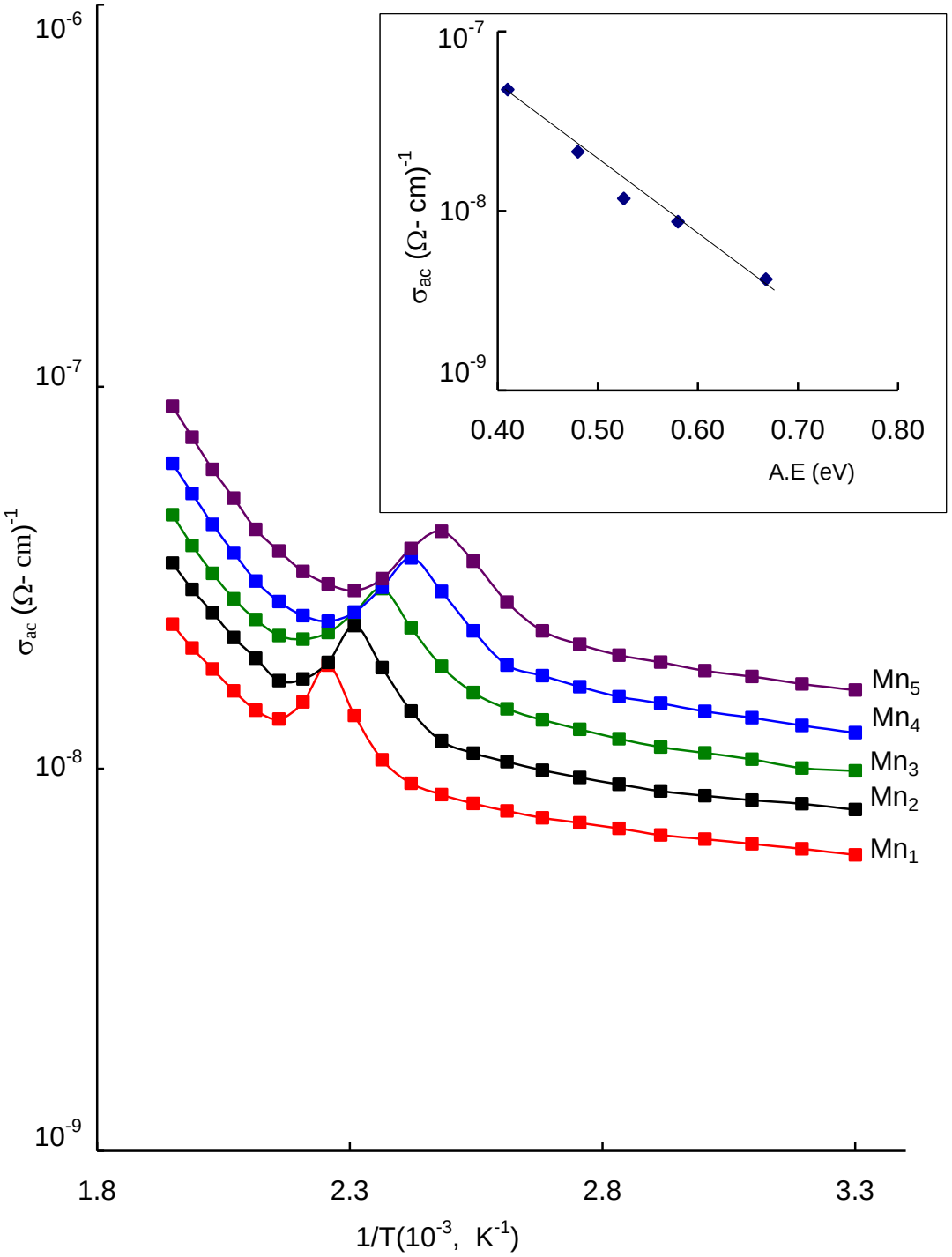


Φιγ. 4.14 ςαριατιον οφ $\sigma_{ac}$ with 1/T at 100 kHz of $PbO\text{-}Sb_2O_3\text{-}As_2O_3$: MnO glass ceramics. Inset represents the variation of a.c. conductivity with activation energy for conduction.

## 4.5 Discussion

Among various constituents of PbO- $Sb_2O_3$-$As_2O_3$: MnO glass ceramic, $As_2O_3$ is a strong network former and participate in the glass network with corner sharing $AsO_3$ pyramidal units; further, there is a possibility for the cross linking of a part of $SbO_3$ units with $As^{3+}$ ions to form Sb-O-As bonds in the glass network; this is reasonable because the ionic radii of $As^{3+}$ (~ 0.70 Å) and $Sb^{3+}$ (~ 0.90 Å) are not very different from each other. The presence of common meta-centers of $\nu_2$ and $\nu_3$ vibrational bands in the ranges of 615–630 $cm^{-1}$ and 760–775 $cm^{-1}$ respectively of $SbO_3$ and $AsO_3$ structural units, in the IR spectra of the glass ceramics in fact supports such a view point. However, earlier EXAFS studies indicated that $Sb^{V}O_4$ units are more compatible in the network forming rather than $SbO_3$ trigonal pyramids units to form linkages with the conventional $AsO_3$ structural units [51]. The reasons are obvious; $Sb^{3+}$ ion with its lone electron pair occupies a greater angular volume than a bonding pair of electrons. As a participant of glass network, the local structure of $Sb^{3+}$ cations become less symmetric and the strain energy in the glass network increases as a whole, thus resulting in a decrease in the additional activation energy that is necessary for glass network rearrangement. As a result we expect that more degree of disorder in glasses containing $Sb^{3+}$ ions rather than in the glasses containing $Sb^{5+}$ ions.

PbO in general is a glass modifier; however, it may participate in the glass network with [$PbO_{4/2}$] pyramidal units connected in puckered layers.

Normally, manganese ions are expected to exist in $Mn^{2+}$ state in PbO-$Sb_2O_3$-$As_2O_3$ glass network. The electronic configuration of $Mn^{2+}$ ion is $3d^5$, which corresponds to a half filled d shell. Most of the $Mn^{2+}$ complexes are octahedral, and have a high spin arrangement with five unpaired electrons [52]. The presence of these ions in tetrahedral positions is also reported in a number of glass systems [53]. These tetrahedrally positioned manganese ions occupy network forming positions with $MnO_4$ structural units and may form linkages with the other network formers. The presence of lead ions in PbO-$Sb_2O_3$-$As_2O_3$ glass network may provide oxidizing environment to get converted a fraction of $Mn^{2+}$ ions in to $Mn^{3+}$ ions during melting and crystallization processes.

In general, the structural compactness, the modification of the geometrical configuration of the glassy network, the change in the coordination of the glass forming ions and the fluctuations in the dimensions of the interstitial holes are the factors that influence the density of the glass ceramic material. The progressive introduction of crystallizing agent MnO caused a slight decrease in the density especially of the samples crystallized with higher concentrations of MnO; this is an indicative of decreasing

structural compactness of the material. The decreasing concentration of $Sb^{5+}$ ions may also be responsible for such reduction in the density.

X-ray diffraction pattern of these samples indicate the presence of $Pb_5Sb_2O_8$, $PbSb_2O_6$, $SbAsO_4$, $Mn_2Sb_2O_7$, $Mn_3Sb_2O_6$, $Mn_2O_3$, $MnAsO_4$ and $Pb_5Sb_4O_{11}$ crystalline phases as mentioned earlier. In manganese rich glasses, the presence of $Mn_2O_3$, $MnAsO_4$ crystalline phases in which manganese ions exist in $Mn^{3+}$ state, are also detected. These meta stable crystals are usually in solid-solution phases and contain the major constituents of the glass composition in the approximately same proportion as they were present in the original glass matrix. This type of separation of various phases may lead to a Mn fortification of the droplet, leaving the glass matrix with a very low content of manganese. The Mn rich areas in the glass may enhance the reactivity of Mn with the other oxides that precipitate as high density of fine Mn rich crystals. These tiny crystals act as heterogeneous nuclei for the crystallization of the remaining glass. The diffraction peaks corresponding to $PbSb_2O_6$, $SbAsO_4$ crystalline phases seem to be slowly faded away as the content of the crystallizing agent is increased; this observation indicates that the concentration of $Sb^{5+}$ ions is marginal in the samples crystallized with higher concentration of MnO.

The appearance of different crystallization temperatures in the DTA pattern obviously suggests the presence of different phases of crystallization in the samples. The crystallization in these samples may take place following the surface and bulk nucleations. The shape of the crystallization peaks in DTA curves suggests an increase of enthalpy with increase in the concentration of crystallizing agent; this observation suggests that the crystallization starts initially inside the material and expands to the surface gradually [54]. The shifting of maximum mass reduction temperature (TGA) towards lower side with increase in the concentration of nucleating agent suggests the growing degree of disorder with increase in the concentration of MnO.

The decrease in the intensity of the bands due to symmetric stretching and bending vibrations of $AsO_3$ and $SbO_3$ structural units in the IR spectra with increase in the concentration of the crystallizing agent MnO clearly suggests an increasing modifying action of these ions. It may be noted here that it is the octahedral ion that induce more non-bridging oxygens and structural disorder in the glass network. Hence, the analysis of IR spectral studies of the samples points out that there is a gradual transformation of manganese ions from tetrahedral to octahedral positions.

By diagonalising the energy matrices for $d^5$ configuration, the clearly resolved band observed at about 520 nm in the optical absorption spectra of $PbO\text{-}Sb_2O_3\text{-}As_2O_3$: MnO glass ceramics is assigned to $^6A_{1g}(S) \rightarrow {}^4T_{1g}(G)$ transitions and the crystal field parameter $D_q$ and Racah inter-electronic repulsion parameter B have been determined as 690 $cm^{-1}$ and 782 $cm^{-1}$ respectively. The values of the $D_q$ and B obtained are consistent with the values reported in the literature for number of other glass systems [55-57]. From these values, it may be concluded that the bonding of divalent manganese ions occupy in these glass ceramics is ionic and occupy octahedral positions. The considerably broad band observed at 422 nm can safely be ascribed to $^6A_1(S) \rightarrow {}^4T_2(G)$ transition of tetrahedral $Mn^{2+}$ ions. Further, the growth of the octahedral band at the expense of tetrahedral band suggests that there is a gradual decrease of tetrahedrally positioned $Mn^{2+}$ ions in the glass ceramic. These tetrahedrally positioned manganese ions occupy network forming positions with $MnO_4$ structural units and may form linkages with the other network formers. Simultaneously a well resolved broad band is detected at about 495 nm especially in the spectra of the glasses crystallized with higher concentrations of MnO; this band is attributed to spin allowed $^5E_g \rightarrow {}^5T_{2g}$ transition. The presence of this band suggests that a

part of manganese ions exist in $Mn^{3+}$ ($d^4$) that occupy octahedral positions [46, 47, 57] in the glass ceramic.

The decrease in the optical band gap with the increase in the concentration of the nucleating agent may be explained as follows: the gradual increase in the concentration of octahedrally positioned $Mn^{2+}$ ions, causes a creation of large number of donor centers; subsequently, the excited states of localized electrons originally trapped on $Mn^{2+}$ sites begin to overlap with the unfilled 3d states on the neighboring impurity sites. As a result, the impurity band becomes more extended into the main band gap. This development might have shifted the absorption edge to the lower energy (Table 4.3) which leads up to a significant shrinkage in the band gap.

There are a number of recent papers dealing with luminescence of $Mn^{2+}$ ions in oxide host lattices [2]. In general the $Mn^{2+}$ ions in tetrahedral coordination give luminescence emission at lower wavelengths, whereas the octahedral or distorted tetrahedral coordination emits at higher wavelengths. With these facts we assign the features of green emission band (observed at about 550 nm) due to $^4T_1(^4G) \rightarrow {}^6A_l(^6S)$ tetrahedral transition of $Mn^{2+}$ ions and orange to red emission band due to $^4T_{1g}(^4G) \rightarrow {}^6A_{lg}(^6S)$ octahedral transition of $Mn^{2+}$ ions. The gradual growth of octahedral band at the expense of tetrahedral band clearly suggests the transformation of $Mn^{2+}$ ions

from tetrahedral to octahedral positions and the samples crystallized with 5 mol% of MnO exhibits highest luminescence efficiency.

The ground state of $d^5$ electronic configuration in the free atom is $^6S_{5/2}$ and possesses zero orbital angular momentum. Hence an ESR signal is expected with 'g' value very close to the free electron value 2.0023. Since the total orbital momentum is zero, in the first order there can be no interaction with the crystal field and any higher order interactions must arise from fine structure terms. For $Mn^{2+}$ ion, if we neglect the nuclear Zeeman term, the spin Hamiltonian term can be written as,

$$H = \mu_B gBS + ASI + DS_Z^2 - \frac{1}{3}S(S+1) + E(S_X^2 - S_Y^2) \qquad (4.1)$$

Where $\mu_B$ is the Bohr magneton, g is electronic g factor, B is the Zeeman field, S is $Mn^{2+}$ electronic spin =5/2, I is the $Mn^{2+}$ nuclear spin = 5/2, A is the hyper fine interaction tensor and D and E are non-axial zero field splitting parameters. In case of $d^5$ metal ions, it is known that the axial distortion of octahedral symmetry gives rise to three Kramers doublets $\left|\pm\frac{5}{2}\right\rangle, \left|\pm\frac{3}{2}\right\rangle and \left|\pm\frac{1}{2}\right\rangle$ [58].

An application of Zeeman field will split the spin degeneracy of the Kramers doublets. As the crystal field splitting is normally much greater than the Zeeman field, the resonances observed are due to transitions within the

Kramers doublets split by the Zeeman field. The resonance at g = 2.0 is due to $Mn^{2+}$ ions in an environment close to an octahedral symmetry and is known to arise from the transition between the energy levels of the lower doublet $\left|\pm\frac{1}{2}\right\rangle$. This line with well resolved hyperfine splitting (due to $^{55}Mn$) can be further interpreted in terms of this spin-Hamiltonian described by Eq. (2) by assuming that the parameters of the fine structure D and E are $|D| \cong |E|$ << gβH, i.e., the non-cubic crystalline electric fields (that are contributing to the EPR spectra of these samples) are weak. The signal observed at g = 4.3 corresponding to $|D| \geq g\beta H$ and E/D = l/3 is due to magnetically isolated $Mn^{2+}$ ions in tetragonally (and or rhombically) distorted octahedral sites of symmetry subjected to strong crystal field effects [59], and arises from transitions between the energy levels of the middle Kramers doublet $\left|\pm\frac{3}{2}\right\rangle$. The difference between these levels is higher than the transition energy at 9.205 GHz microwave frequency and hence the intensity of this signal is expected to be low as observed.

The intensity ($\Im$) of the EPR signal is assumed to be proportional to the product of the peak-to-peak height (I) and the square of its width (ΔB) [60]:

$$\Im \approx I(\Delta B)^2 \qquad (4.2)$$

The dependence of this factor, for $g_{eff}$ ~2.0 resonance arising from $Mn^{2+}$ ions is shown as an inset of Fig. 4.9; the figure shows that the intensity of the resonance signal increases with increase in the concentration of nucleating agent MnO. The effective value of g and the hyperfine interaction parameter A (considered as isotropic parameters for $Mn^{2+}$ ion) evaluated from these spectra are reported in Table 4.4. The hyperfine splitting parameter also increases gradually from 9.02 to 9.88 mT with the concentration of the nucleating agent. This observation clearly suggests the increasing ionic nature of the bonding between $Mn^{2+}$ ions and its ligands and ions occupy octahedral positions. The deviation of g from $g_e$ is observed to become gradually negative with increase in the content of MnO, this observation also indicates the increasing concentration of octahedral positioned $Mn^{2+}$ ions. The larger values of g observed for the samples $Mn_2$ and $Mn_3$ are partly due to the contribution of orbital angular momentum to the magnetic moment of $Mn^{2+}$ ions. The fraction of the magnetic moment due to the orbital angular momentum $I_o$ (orb), to that due to spin angular momentum, $I_s$ (spin), may be expressed as follows:

$$I_s / I_o = (g/2)-1 \qquad (4.3)$$

Such an interesting feature can be understood due to strong dipolar interaction, (which is more predominant in the samples with low content of

MnO) that causes a localized magnetic field at the site of $Mn^{2+}$ ion and lead to the high effective g value as observed [61, 62].

The single resonance without hyperfine splitting observed for the samples crystallized with low content of MnO can be attributed to spin-spin interaction between $Mn^{2+}$ ions and its ligands. The low value of hfs constant is also an indicative of more covalent bonding in these samples [63].

The magnetic properties of PbO-$Sb_2O_3$-$As_2O_3$: MnO glass ceramic samples arise from the paramagnetic $Mn^{2+}$ and $Mn^{3+}$ ions. The fairly regular octahedral complexes of these ions are expected to have the magnetic moment ~ 5.90 $\mu_B$ and 4.90$\mu_B$ respectively for $Mn^{2+}$ and $Mn^{3+}$ ions [47]. Using the atomic magnetic moment values of free $Mn^{2+}$ and $Mn^{3+}$, the percentage of divalent and trivalent manganese ions in the glass ceramic matrix has been evaluated approximately from $\mu_{exp}$ using the equation.

$$x\,\mu^2_{exp} = x_1\mu^2_{(Mn^{2+})} + x_2\mu^2_{(Mn^{3+})} \qquad (4.4)$$

with $x = x_1 + x_2$

x is the MnO concentration $x_1$ and $x_2$ are the molar fractions of manganese ions in $Mn^{2+}$ and $Mn^{3+}$ valence states. The values obtained are presented in Table 4.4; the data indicate that there is a significant presence of $Mn^{3+}$ ions in the samples crystallized with higher content of MnO.

**The values of dielectric parameters viz., $\varepsilon'$, tan $\delta$ and $\sigma_{ac}$ at any frequency are found to increase with temperature and activation energy for a.c. conduction is observed to decrease with increase in the content of nucleating agent MnO; this is an indication of an increase in the space charge polarization. Such increase is probably due to the increasing concentration of octahedrally positioned $Mn^{2+}$ ions that act as modifiers in these samples. These modifying ions as mentioned earlier generate bonding defects in the glass network. The defects thus produced create easy path ways for the migration of charges that would build up space charge polarization and facilitate to an increase in the dielectric parameters as observed [64, 65].**

The value of the effective activation energy associated with the dipoles is observed to decrease with increase in the content of manganese ions in the glass ceramic network (Table 4.5), this observation points out an increasing freedom for dipoles to orient in the field direction, obviously due to increasing degree of disorder in glass ceramic network. The observed dielectric relaxation effects in $PbO\text{-}Sb_2O_3\text{-}As_2O_3$ glasses crystallized with different concentrations of MnO may be attributed to the association of octahedrally positioned $Mn^{2+}$ ions with a pair of cationic vacancies as observed in a number of conventional glasses, glass ceramics and crystals that contain divalent positive ions as reported before [66].

The variation of log $\sigma(\omega)$ vs. activation energy for conduction (in the high temperature region) is shown as inset in Fig. 4.14; the graph yields a near straight line. This observation suggests that the conductivity enhancement is directly related to the thermally stimulated mobility of the charge carriers in the high temperature region. The progressive increase of conductivity with the increase of manganese content in the glass ceramic is a manifestation of the increasing concentration of mobile electrons, or polarons, involved in the process of transfer from $Mn^{2+}$ to $Mn^{3+}$. In insulators, where broad distribution of relaxation times $\tau$ exist, like in the present samples, the ac conduction can be represented by

$$\sigma = \sigma_0 \ e^{-\xi} \qquad (4.5)$$

There are two mechanisms that could contribute to the form of Eq. (6) for ac conduction: the first contribution is due to the normal classical activation of a carrier over a potential barrier 'W' separating two sites, in this case $\xi$ = W/KT. This mechanism can be adopted to the simple Debye loss case. Second contribution is due to the tunneling of a carrier through a potential barrier between the sites separated by a distance R, in this case $\xi=2\alpha R$, where $\alpha^{-1}$ being the localization strength; this mechanism is applicable for explaining low-temperature part of the conductivity (nearly temperature-independent part) as described below. The way the ac conductivity varies

with the temperature for the present samples indicate that both the mechanisms are responsible for ac conduction, in $PbO\text{-}Sb_2O_3\text{-}As_2O_3$: MnO glass ceramics. The low temperature part of the conductivity (a near temperature independent part, as in the case of present glass ceramics up to nearly 70 $^oC$) can be explained on the basis of quantum mechanical tunneling model [67] as reported in a number of our earlier papers [68, 69]. Based on quantum mechanical tunneling model, $N(E_F)$ is the density of the energy states near the Fermi level have been evaluated and values obtained are presented in Table 4.6. The value of $N(E_f)$ obtained $\approx 10^{20}$ $eV^{-1}$ $cm^{-3}$; such values of $N(E_F)$ suggest the localized states near the Fermi level are responsible for conduction. Further, the value of $N(E_F)$ is found to increase gradually from the sample $Mn_1$ to sample $Mn_5$, indicating an increase in the degree of disorder in the glass network.

## 4.6 Conclusions

$PbO\text{-}Sb_2O_3\text{-}As_2O_3$ glasses have been crystallized with different concentrations of MnO. The scanning electron microscopic studies indicated that the samples contain well defined and randomly distributed crystal grains. The X-ray diffraction studies have revealed the formation of different crystalline phases with $Sb^{3+}$, $As^{3+}$, $Sb^{5+}$, $Mn^{2+}$, $Mn^{3+}$ and $Pb^{2+}$ ions as constituents. The study of DTA suggests the crystallization spreads from

inside to the surface of the samples and also indicated the presence of the different crystalline phases. The IR spectral studies indicated the decreasing concentration of $AsO_3$ and $SbO_3$ symmetrical structural vibrational groups with increase in the concentration of MnO. The optical absorption and luminescence spectra of $PbO\text{-}Sb_2O_3\text{-}As_2O_3$ glass ceramics exhibit bands due to the transitions of tetragonally and octahedrally positioned $Mn^{2+}$ ions. In addition, the traces of $Mn^{3+}$ ions could also be detected from these studies. The presence of $Mn^{3+}$ ions is also confirmed from magnetic susceptibility studies. ESR spectral studies have indicated that the bonding of manganese ions with ligands is mostly ionic in nature especially in the samples containing higher content of MnO. These studies have also indicated that with increase in the concentration of nucleating agent, there is a gradual transformation of manganese ions from tetragonal to octahedral coordination. The analysis of the results of dielectric studies suggests a decrease in the insulating character with increase in the crystallizing agent of these samples.

## References


1. A. Murali, R.P. Sreekanth Chakradhar, J. Lakshmana Rao, *Physica B* 358 (2005) 19.

2. Tomoe Sanada, Kazuhiro Yamamoto, Noriyuki Wada, Kazuo Kojima, *Thin Solid Films* 496 (2006) 169.

3. I.E.C. Machado, L. Prado, L. Gomes, J.M. Prison, J.R. Martinelli, *J.Non-Cryst. Solids* 348 (2004) 113.

4. I. Ardelean, Simona Cora, Raluca Ciceo Lucacel, Octavia Hulpus, *Solid State Sci.* 7 (2005) 1438.

5. I. Ardelean, M. Peteanu, I. Todor, *Phys. Chem. Glasses* 43 (2002) 276.

6. I. Ardelean, M. Peteanu, S. Filip, V. Simon, I. Todor, *Solid State Commun*. 105 (1998) 339.

7. M. Srinivasa Reddy, G. Murli Krishna, N. Veeraiah, *J. Phys. Chem. Solids* 67 (2006) 789.

8. G. Srinivasarao, N. Veeraiah, *J. Alloys Compd*. 327 (2001) 52.

9. D.K. Durga, N. Veeraiah., *J. Phys. Chem. Solids* 64 (2003) 133.

10. A. Patra, Gary A. Baker, Sheila N. Baker, *J. Lumin*. 111 (2005) 105.

11. C.R. Ronda, T. Amrein, *J. Lumin.* 69 (1996) 245.

12. R. Reisfeld, A. Kisilev, C.K. Jorgensen, *Chem. Phys. Lett*. 111 (1984) 19.

13. M. Eyal, R. Reisfeld, A. Schiller, C. Jacobonic, C.K. Jorgensen, *Chem. Phy. Lett.* 140 (1987) 595.

14. A.J. Faber, A. Van Die, G. Blasse, F. Van der Weg, *Phys. Chem. Glasses* 28 (4) (1987) 150.

15. A.P. Vink, M.A. de Bruin, S. Roke, P.S. Peijzel, A. Meijerink, *J. Electro chem. Soc*. 148 (2001) E313.

16. G. Ajith Kumar, P.R. Biju, Gin Jose, N.V. Unnikrishnan, *Mat. Chem. Phys*. 60 (1999) 247.

17. P.I. Paulose, G. Jose, V. Thomas, N.V. Unnikrishnan, M.K.R. Warrier, *J. Phys. Chem. Solids* 64 (2003) 841.

18. U Caldi˜no, J L Hern´andez-Pozos, C Flores, A Speghini, M Bettinelli, *J. Phys. Condens. Matter* 17 (2005) 7297.

19. S. Parke, A.I. Watson, R.S. Webb, *J. Phys. D: Appl. Phys*. 3 (1965)763.

20. A. Bingham, S. Parke, *Phy. Chem. Glasses* 6 (1965) 224.

21. D.E. Wortman, C.A. Morrison, *Opt. Mater*. 4 (1995) 487.

22. I. Bratu, I. Ardelean, A. Barbu, V. Mih, D. Maniu, G. Botezan, *J. Mol. Structure* 482 (1999) 689.

23. L.E. Orgel, *J. Chem. Phys.* 23 (1955) 1824,1958.

24. S. Parke, R.S. Webb, *Phys. Chem. Glasses* 13 (1972)157.

25. D. Simkin. K. Oyama-Gannon, P. Menassa and P. Taylor, *J. Lumin*. 24 (1981) 107.

26. B.Andrianasolo, B. Champagnon, E. Duval, *Phys. Chem. Glasses* 30 (1989) 215.

27. I. V. Kityk, *J. Phys. Chem. B* 107 (2003) 10083.

28. J. C. Sabadel, P. Armand, D. Cachau-Herreillat, P. Baldeck, O. Doclot, A. Ibanez and E. Philippot, *Solid State Chem.* 132 (1997) 411.

29. Marcelo Nalin, Marcel Poulain, Michel Poulain, J. L. Ribeiro Sidney and Younes Messaddeq *J. Non-Cryst. Solids* 284 (2001) 110.

30. J. S. Wang, E. M. Vogel, E. Snitzer *Opt. Mater.* 3 (1994) 187.

31. T. Satyanarayana, I. V. Kityk, K. Ozga, M. Piasecki, P. Bragiel, M. G. Brik, V. Ravi Kumar, N. Veeraiah, A. H. Reshak, *J. Alloys and Comp.* 482 (2009) 283.

32. R.M. Krishna, J.J. Andre, J.L. Rao, W.E. Antholine, *Mater. Res Bull.*34 (1999) 1521.

33. L.D. Bogomolova, N.A. Krasil'nikova and V.V. Mitrofanov, *J. Non-Cryst. Solids* 188 (1995) 130.

34. A.Van Die, A.C.H. ILeenaers, G. Blasse and W.F. Van Der Weg, *J. Non-Cryst. Solids* 99 (1988) 32.

35. D. Jean Michel, J. Videau and J. Portier, *J. Non-Cryst. Solids* 86 (1986) 88.

36. E. Baiocchi, A. Montenero, M. Bettinelli, *J. Non-Cryst.Solids* 46 (1981) 203.

37. J. Jethwa, F.P. Schafer and R. Reisfeld, *Appl. Phys. B.* 50 (1990) 231.

38. I. Kashif, *J .Mater. Sci. Mater. Electron.* 1 (1990) 49.

39. I.M. Wang and X. Fan, *J. Chin. Ceram. Soc.* 23 (1995) 61.

40. J. L.Rao, B. Sreedhar , S.V.J. Lakshman, *J. Non-Cryst. Solids* 92 (1987) 175.

41. Chengyu Li, Yingning Yu, Shubing Wang, Qiang Su *J. Non- Cryst. Solids 321 (2003) 191.*

42. R. Stefan and S. Simon, *Mod. Phys.Lett.* 3 (2000) 111

43. R. Dummy, *J. Non-Cryst. Solids* 41 (1980) 273.

44. A. S. Rao, B. Sreedher, J. L. Rao, *J. Non-Cryst. Solids* 144 (1992) 169.

45. M. Srinivasa Reddy, G. Murali Krishna and N. Veeraiah, *J. Phys. Chem. Solids* 67 (2006) 789.

46. F. A. Cotton, G. Willkinsin, *Advanced Inorg. Chem.* Wiley-Eastern, New Delhi, 1976.

47. I. Ardelean, M. Peteanu, V. Simon, F. Ciorcas, C. Bob, *Mater. Lett.* 39 (1999) 42

48. A. Bishay, C. Maghrabi, *Phys. Chem. Glasses* 10 (1969) 1.

49. B. Dubois, J. J. Videau, M. Couzi, J. Portier, *J. Non-Cryst. Solids* 88 (1986) 355

50. P. Subbalakshmi, P. S. Sastry, N. Veeraiah, *Phys. Chem. Glasses* 42 (2001) 307.

51. D. Holland, *Solid State NMR* 26 (2004) 72.

52. R. K. Brow, D. R. Tallent, S. T. Myers, *J. Non-Cryst. Solids* 191 (1995) 45.

53. A. Radu, L. Baia, W. Kiefer, S. Simon, *Vibrational Spectroscopy* 39 (2005) 127.

54. A. Marotta, A. Buri and F. Branda, *J. Mater. Sci.* 16 (1981) 341.

55. Y. Suzuki and W. A. Sibley, *Phys. Rev. B* 35 (1987) 4472.

56. L. N. Feuerhelm, S. M. Sibley, W. A. Sibley, *J. Solid State. Chem.* 54 (1984) 164.

57. R. P. Sreekanth Chakradhar, G. Sivaramaiah, J. Lakshmana Rao, N. O. Gopal, *Spectrochim. Acta Part A* 62 (2005) 761.

58. A. Abragam, B. Bleaney, *Electron Paramagnetic Resonance of Transition Ions,* Clarendon Press, Oxford, 1970.

59. L. D. Bogomolova, Yu. G. Tepliakov, F. Caccavale, *J. Non-Cryst. Solids* 194 (1996) 291.

60. I. Bratu, I. Ardelean, A. Barbu, V. Mih, D. Maniu, G. Botezan, *J. Mol. Structure* 482 (1999) 689.

61. K. Shingawa, S. Taniguchi, *Jpn. J. Appl. Phys.* 13 (1974) 1664.

62. N. Krishna Mohan, M. Rami Reddy, N. Veeraiah, *J. Alloys Comp.* 458 (2008) 66.

63. R. M. Krishna, J. J. Andre, J. L. Rao and W. E. Antholine, *Mater. Res. Bull.* 34 (1999) 1521.

64. G. Murali Krishna, M. Srinivasa Reddy and N. Veeraiah, *J. Solid State Chem.* 180 (2007) 2747.

65. L. Srinivasa Rao, M. Srinivasa Reddy, D. Krishna Rao and N. Veeraiah, *J. Solid State Sci.* 11 (2009) 578.

66. V. R. Kumar, N. Veeraiah and S. Buddudu *J. de Phys. III* 7 (1997) 951.

67. I.G. Austin, N.F. Mott, *Adv. Phys.* 18 (1969) 657.

68. G. Little Flower, M. Srinivasa Reddy, M. V. Ramana Reddy and N. Veeraiah, *Z. Naturforsch.* 62a (2007) 315.

69. G. Sahaya Baskaran, D. Krishna Rao and N. Veeraiah, *Solid State Commun.* 145 (2008) 401.